Magnetic Helicity Injection by Horizontal Flows in the Quiet Sun: I. Mutual Helicity Flux

B.T. Welsch[1]

Space Sciences Laboratory, University of California, Berkeley, CA 94720-7450; welsch@ssl.berkeley.edu

D.W. Longcope

Physics Department, Montana State University, Bozeman, MT 59717-3840;dana@physics.montana.edu

ABSTRACT

The flux of magnetic helicity through the solar photosphere has implications in diverse areas of current solar research, including solar dynamo modelling and coronal heating. In this work, we focus on the flux of magnetic helicity from quiet-sun magnetic fields. We express the total helicity flux in terms of mutual- and self-helicities, which arise from relative motions of separate flux elements, and from internal motions within individual magnetic flux elements, respectively. Using a novel labelling algorithm and a tracking algorithm applied to high cadence, high resolution SOHO/MDI magnetograms, we determine the observed mutual helicity flux density in the quiet sun to be $\sim 5 \times 10^{12} \mathrm{Mx}^2 \mathrm{cm}^{-2} \mathrm{s}^{-1}$, and compare this value with a simple theoretical prediction. The observed rate corresponds to a whole-cycle, hemispheric mutual helicity flux of $\sim 10^{43} \mathrm{Mx}^2$ from the quiet sun, meaning helicity injection by surface motions in quiet sun fields is neglible compared to the active region helicity flux rate.

Subject headings:

1. Introduction

Magnetic helicity has been widely recognized as a useful tool in the study of solar magnetic fields (see, e.g., Rust's 2002 review, and references therein). Within a finite volume

---

[1]Physics Department, Montana State University, Bozeman, MT 59717-3840

V, whose boundary is not a flux surface, the term "helicity" generally refers to the guage-invariant relative helicity (Berger and Field 1984). The relative helicity can be expressed as the integral (Finn and Antonsen 1985),

$$\mathcal{H} = \int_V d^3x \, (\mathbf{A} + \mathbf{A}_P) \cdot (\mathbf{B} - \mathbf{B}_P) \quad , \tag{1}$$

where $\mathbf{B}_P$ is the unique potential magnetic field matching the normal component of actual field $\mathbf{B}$ at the boundary, and $\mathbf{A}$ and $\mathbf{A}_P$ are vector potentials generating $\mathbf{B}$ and $\mathbf{B}_P$, respectively. The relative helicity is defined to be zero for a potential field.

Within a highly conducting plasma, the relative helicity is approximately conserved (Taylor 1974), and may change only through fluxes across the boundary surface S (Berger and Field 1984),

$$\frac{d\mathcal{H}}{dt} = 2 \int_S d\mathbf{a} \cdot \left[(\mathbf{A}_P \cdot \mathbf{B})\mathbf{v} - (\mathbf{A}_P \cdot \mathbf{v})\mathbf{B} \right] \quad , \tag{2}$$

where $d\mathbf{a}$ points into V.

The overall budget of coronal helicity has significance for several aspects of solar magnetism. Helicity can serve as a proxy for free magnetic energy (energy above that of the potential field), so a net helicity flux is a proxy for heating. Strict helicity conservation poses an obstacle to several dynamo models (Boozer 1999), which might be removed if helicity were to escape into the heliosphere. Finally, both remote and *in situ* observations (Zirker *et al.* 1997; Smith 1999) indicate that the coronal and heliospheric fields in each hemisphere have net helicity, implying some helicity flux through the photosphere.

Several efforts have recently been made to predict theoretically and to quantify observationally the photospheric helicity flux in active region fields. DeVore's (2000) theoretical work indicates that the helicity flux from differential rotation advecting a passive active region (with unsigned flux 2Φ) depends on orientation, peaking at $d\mathcal{H}/dt \simeq 0.003\Phi^2$ per day when tilted $30°$ from East-West. Observational studies show this to be far too low to account for the helicity flux into the heliosphere (Demoulin *et al.* 2002a; Green *et al.* 2002). Furthermore, direct measurements of $d\mathcal{H}/dt$ using expression (2) differ markedly in sign, magnitude, and time history from the hypothized passive advection by differential rotation (Chae 2001; Kusano *et al.* 2002).

While active regions are the most obvious surface fields, they are unevenly distributed over the Sun and vary periodically according to the solar cycle. If the total helicity flux had similar variations there would be implications for each hemisphere's overall helicity budget. The full extent to which the helicity budget varies will, however, depend on other avenues of helicity flux, most notably the flux thorugh the quiet sun magnetic field. The present work is the first to quantify the helicity flux through the quiet sun.

The quiet Sun's photospheric field consists of numerous small ($\Phi \sim 3 \times 10^{18}$ Mx; Schrijver *et al.* 1997) magnetic elements of mixed polarity, generally found along the network of supergranule boundaries. With $\sim 10^4$ such elements present at any time, the unsigned flux in quiet Sun fields is comparable to or greater than that in active regions. Some results (LaBonte and Howard 1982) suggest that the distribution of elements varies little with latitude or solar cycle (at least away from the poles), so it is possible for the quiet sun to provide a more uniform and constant helicity flux than active regions.

The next section derives the expression for helicity flux through a quiet-sun field composed of discrete photospheric elements. This is found to consist of a mutual helicity contribution, due to the interwinding of element pairs, and a self helicity contribution, due to the internal motions of individual elements. We use this expression to derive a theoretical mutual helicity flux by assuming a random arrangement of sources moving according to differential rotation. This theoretical estimate is then tested observationally in the following two sections. Section 3 describes a method of analyzing a sequence of magnetograms to measure the quiet sun mutual helicty flux. This technique is applied to three different data sets from SOI/MDI (Scherrer *et al.* 1995), to calculate the mutual helicty flux in particular quiet sun areas. The results of these measurements are presented in section 4. The final section summaries our results and discusses their implications for the Sun's overall helicity budget.

2. Theory of Helicity Transport

2.1. The Flux of Relative Helicity

We label the two terms in equation (2), from left, the emergence and braiding terms. The former corresponds to the advection of fields already containing magnetic helicity across the boundary surface, while the latter corresponds to the braiding of footpoints of already-emerged fields that thread the boundary surface.

Recent work by Démoulin and collaborators (Demoulin *et al.* 2002b; Demoulin *et al.* 2002a) suggests that the dominant source of active region helicity flux into the corona is the inherent twist present in emerging fields. Precisely quantifying the emergence contribution requires knowledge of both the tangential magnetic field and the normal velocity field at the photospheric boundary surface (Kusano *et al.* 2002). We, however, are primarily concerned with quiet-sun magnetic fields, in which measurements of the tangential field components are noisy. Further, high-cadence, long-duration data sets are not readily obtainable. For these reasons, we cannot accurately quantify the emergence rate of magnetic helicity in the quiet sun, and neglect its contribution to the total quiet sun helicity flux.

Accordingly, we focus solely on the braiding term in equation (2), assuming

$$\frac{d\mathcal{H}}{dt} = -2\int_S da(\mathbf{A}_P \cdot \mathbf{v})B_z \quad , \tag{3}$$

where we approximate the photosphere as a plane, with $\hat{z}$ being the normal vector into the corona.

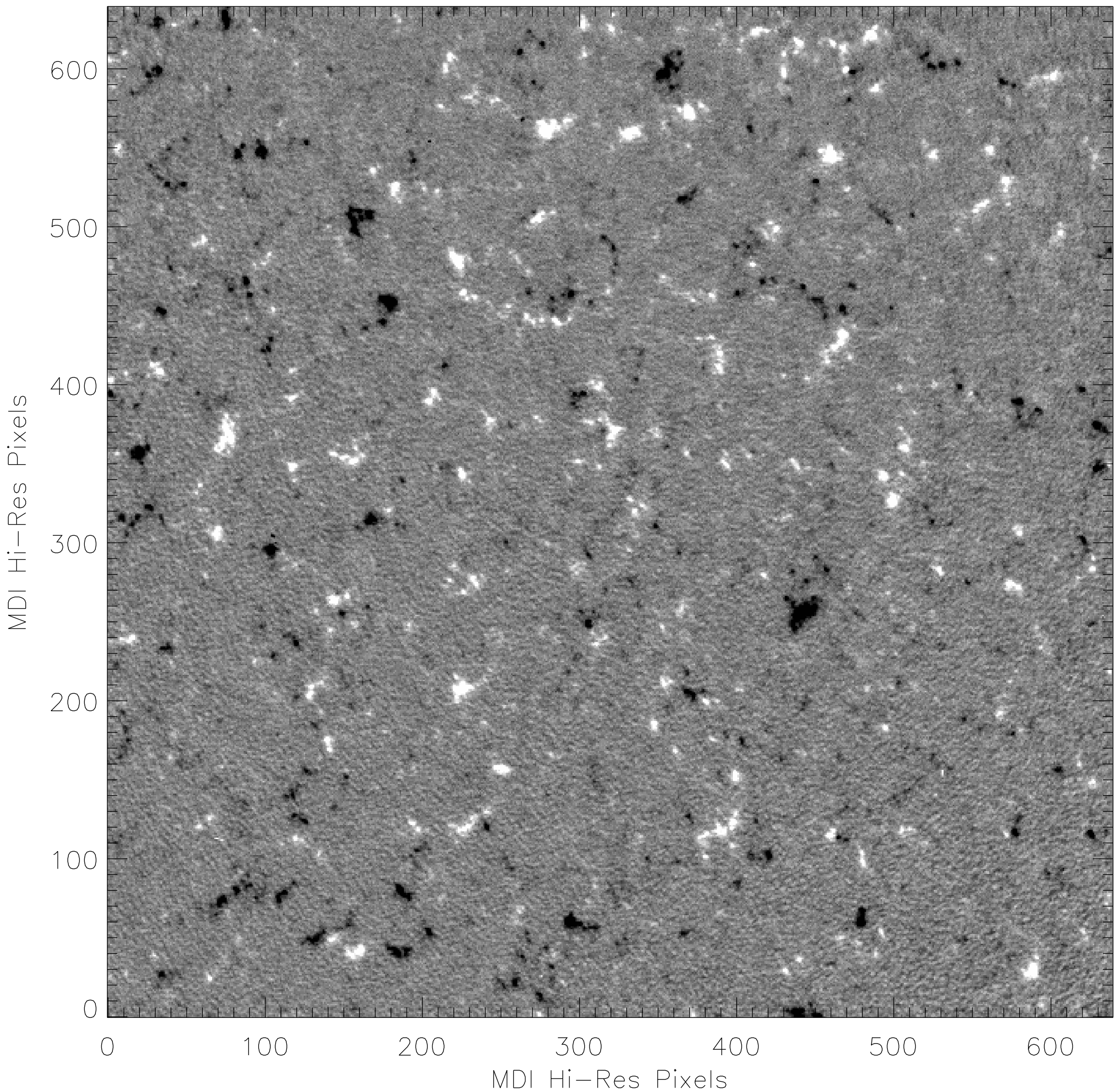

Fig. 1.— The first contrast-enhanced, unsmoothed, five-magnetogram average image from data set # 1. Each tick mark denotes 10 MDI hi-res (.61 ” on a side) pixels. A small active region to the left (east) of this field of view (FOV) was cropped from the full image.

In the quiet sun, the photospheric magnetic field is nonzero only in small, isolated regions. The image in Figure 1, the line-of-sight magnetic field as measured by the Michelson Doppler Imager (MDI) on the Solar and Heliospheric Observatory (SOHO) in its high-resolution (hi-res) mode (Scherrer *et al.* 1995), exemplifies this. Consequently, we can accurately approximate the normal magnetic field B_z at the photosphere as arising from N point-like sources.

We define the normalized, flux-weighted average position of the ith source (its magnetic center of flux) in the usual way,

$$\bar{\mathbf{x}}_i \equiv \frac{1}{\Phi_i} \int_{S_i} d^2x \, B_z(\mathbf{x}) \quad , \tag{4}$$

where S_i is the area covered by the ith source. So

$$B_z(\mathbf{x}) = \sum_{i=1}^{N} \Phi_i \, \Delta_i(\mathbf{x} - \bar{\mathbf{x}}_i) \quad , \tag{5}$$

where $\Delta_i(\mathbf{x} - \bar{\mathbf{x}}_i)$ is the distribution of flux in the ith source, and is strongly peaked near $\bar{\mathbf{x}}_i$ and zero far away.

In Coulomb gauge, the vector potential for the current-free magnetic field $\mathbf{B}_P$, evaluated on the surface, is then

$$\mathbf{A}_P(\mathbf{x}) = \sum_{i=1}^{N} \frac{\Phi_i}{2\pi} \int_{S_i} da' \Delta_i(\mathbf{x}' - \bar{\mathbf{x}}_i) \frac{\hat{z} \times (\mathbf{x} - \mathbf{x}')}{|(\mathbf{x} - \mathbf{x}')|^2} = \sum_{i=1}^{N} \mathbf{A}_P^{(i)}(\mathbf{x}) \quad , \tag{6}$$

where we have implicitly defined the vector potential due to the ith flux element, $\mathbf{A}_P^{(i)}$. Inserting these expressions into equation (3) and pulling out the $i = j$ term in the double summation results in an expression for the helicity flux with self and mutual terms (Berger 1999),

$$\begin{aligned} \frac{d\mathcal{H}}{dt} &= \underbrace{-2 \sum_{i=1}^{N} \Phi_i \int_{S_i} da (\mathbf{v} \cdot \mathbf{A}_P^{(i)}) \Delta_i(\mathbf{x} - \bar{\mathbf{x}}_i)}_{\text{self}} \\ &+ \underbrace{\left(-2 \sum_i \sum_{j \neq i} \Phi_j \int_{S_j} da (\mathbf{v} \cdot \mathbf{A}_P^{(i)}) \Delta_j(\mathbf{x} - \bar{\mathbf{x}}_j) \right)}_{\text{mutual}} \quad . \end{aligned} \tag{7}$$

The self term arises from braiding of field lines within a single flux element, while the the mutual term arises from braiding of field lines from different flux elements. In this paper, we concern ourselves only with the mutual helicity flux term. In a subsequent paper, currently in preparation, we build upon this derivation to find the self helicity from non-axisymmetric flux elements, thereby generalizing the helicity flux expression presented in Berger's (1999) review.

2.2. Mutual Helicity Flux

Since $i \neq j$ by assumption in the mutual helicity flux term, we are dealing with fluxes in distinct locations, and we can approximate the flux distribution functions Δ_i in (5) with Dirac δ-functions at the locations $\bar{\mathbf{x}}_i$. The resulting integrations in each $\mathbf{A}_P^{(i)}$ are simple, and yield circumferential vector potentials for each source, meaning the full expression for the mutual helicity becomes

$$\frac{d\mathcal{H}}{dt} \simeq -\frac{1}{\pi} \sum_i \sum_{j \neq i} \Phi_i \Phi_j \Omega_{ij}(\mathbf{x}_i, \mathbf{x}_j) \ , \tag{8}$$

where

$$\Omega_{ij}(\mathbf{x}_i, \mathbf{x}_j) \equiv \Big(\mathbf{v}(\bar{\mathbf{x}}_j) - \mathbf{v}(\bar{\mathbf{x}}_i) \Big) \cdot \frac{\hat{z} \times (\bar{\mathbf{x}}_j - \bar{\mathbf{x}}_i)}{|(\bar{\mathbf{x}}_j - \bar{\mathbf{x}}_i)|^2} \tag{9}$$

is the angular velocity of the jth flux element about the ith. We therefore find the mutual helicity flux from each pair of fluxes to be

$$\frac{d\mathcal{H}_{ij}}{dt} \equiv -\frac{2}{\pi} \Phi_i \Phi_j \Omega_{ij} \quad , \tag{10}$$

where i and j are fixed.

The negative sign means that winding a pair of oppositely-signed fluxes in the right-hand sense, with respect to $\hat{z}$, leads to a positive flux of helicity, while right-handed braiding of two fluxes of the same sign causes a negative flux of helicity.

2.3. Expected Mutual Helicity Flux

The photospheric differential rotation systematically winds magnetic fluxes at different latitudes about each other. In the northern hemisphere, for instance, fluxes wind about each other in a right-hand sense, with respect to a radial normal vector. We now make a rough estimate of the average quiet-sun mutual-helicity flux, $\langle d\mathcal{H}/dt \rangle$, from this effect.

Given a distribution of $2N$ magnetic flux elements, N_+ of flux $+\Phi_0$ and N_- of flux $-\Phi_0$, with $N = N_+ = N_-$, uniformly distributed over a surface area A, the average spatial probability distribution of fluxes is constant, $\mathcal{P}_\pm(\mathbf{x}) = N/A$.

The total expectation value of the mutual helicity flux is the sum of the expectation values from all pairings, each of which is given by an integration over the rotation profile, weighted by $\mathcal{P}_{\pm}(\mathbf{x})$. Most terms in the sum cancel, as there are nearly as many homogenous (+/+ and -/-) pairings ($2N^2 - 2N$) as there are heterogenous (+/- and -/+) pairings ($2N^2$), and they differ only in sign. Thus, we are left with

$$\langle \frac{d\mathcal{H}}{dt} \rangle = 2N \Big(\frac{\Phi_0^2}{\pi} \Big) \frac{1}{A^2} \int dA_i \int dA_j \Omega_{ij}(\mathbf{x}_i, \mathbf{x}_j) = H_0 \overline{\Omega} \ , \tag{11}$$

where we have implicitly defined a characteristic helicity, $H_0 = 2N\Phi_0^2/\pi$, and an average relative rotation rate, $\overline{\Omega}$.

In accordance with the observations of Schrijver et al. (1997) and this work (see below), we assume a typical flux size of $\Phi_0 \sim 3 \times 10^{18}$ Mx, giving a characteristic helicity $H_0/N \sim 10^{37}\mathrm{Mx}^2$ per pair of fluxes.

We estimate $\overline{\Omega}$ from an expansion of the rotation rate in the vertical position in a plane-parallel approximation to the photosphere in MDI's field of view (FOV). For most of the FOV's in our study (see below), we find $\overline{\Omega} \sim 3 \times 10^{-7}\mathrm{rad\ s}^{-1}$, using Snodgrass' (1983) rotation rates for the magnetic photosphere.

The expected rate of mutual helicity flux through the MDI FOV is then $\langle d\mathcal{H}/dt \rangle_{\mathrm{FOV}} \sim 10^{32}\mathrm{Mx}^2\mathrm{s}^{-1}$, where we have estimated that the number of pairs of flux elements in the FOV to be $N = 100$. A typical FOV contains $\sim 5 \times 10^5$ pixels, each 440 km on a side, meaning we predict a helicity flux density on the order of

$$\langle \frac{d\mathcal{H}}{dt} \rangle \sim 10^{11}\mathrm{Mx}^2\mathrm{s}^{-1}\mathrm{cm}^{-2} \quad . \tag{12}$$

3. Methods

3.1. Data

We analyzed SOHO/MDI magnetograms for the photospheric magnetic field B_z used in our study. The instrument finds the line-of-site magnetic field by inverting the Stokes V profile in the Ni I (6768 Å) line, which is formed at the photosphere (Scherrer *et al.* 1995). The datasets analyzed were all taken in the instrument's hi-res mode, with .61" pixels. At SOHO's position at the L1 point between the Earth and the Sun, this corresponds to about 440 km on the Sun.

We tracked fluxes in five archival magnetogram sequences for 7.5 hours or longer, in regions of predominantly quiet sun near solar minimum. Three data sets were taken from the same SOHO observing campaign; we label these sets #2a, #2b, and #2c. Data sets #1 and #3 were also tracked by Hagenaar *et al.* (1999), which allows comparison between some of our results and theirs. The observing times, durations, and pointings of the tracking runs are listed in Table 1.

To improve the signal-to-noise ratio in our data, we average five good magnetograms, usually with 1 minute cadence. Occasionally, however, missing or bad magnetograms increase the time between averaged images. We define a bad magnetogram as one in which more than 1000 pixels are either labelled blank, or exceed 800 G in absolute value; these are simply skipped over in finding five magnetograms to average. Thus, our measurements of the magnetic field have a nominal time resolution of 5 minutes. The time stamp recorded with the pointing information for each averaged set of magnetograms is the average time of observation for the magnetograms; this avoids timing errors due to data gaps from missing or bad magnetograms. Two small active regions present in data sets # 1 and # 3 were cropped in the tracked data. (The field of view shown in Figure 1 is that actually used.)

After averaging, the data are smoothed over ~ 3 pixels, by convolution with a potential extrapolation filter: the kernel is the geometrical contribution to the vertical component of the potential field at $h = 3$ pixels above the photosphere,

$$k(x, y) = \frac{h}{(h^2 + x^2 + y^2)^{(3/2)}} \quad , \tag{13}$$

assuming the measured fields correspond to point monopoles located at the pixel centers.

To estimate the noise in the measurements, we construct a histogram of the field strengths from the smoothed data. We then fit the core region (± 2 G from zero) with a Gaussian, under the assumption that the signal in the core arises entirely from random error. We take the error per pixel for all pixels to be the fitted σ_n; values of σ_n for the data sets are given in Table 1.

An imbalance in the distribution of field strengths displaces the centroid, B_0, of the fit from zero. Following Hagenaar *et al.* (1999), we shift the data in all pixels by $-B_0$. In all cases studied, the magnitude of the shift was below the noise, and in most cases, the shift was around 1/10th of the noise level.

Table 1. Data Set Parameters

Data Set	Start Date, $hh:mm$	Steps Tracked[a]	Size (.61" pixels)[b]	Pointing[c] (deg)[d]	Carrington Rotation[c]	σ_n[c] (G)	B_0[c] (G)
1	1996 Aug 15, 06:22	180	640×640	$(21.0, 8.2)$	1912.7480	1.65	-0.130
2a	1996 Oct 17, 16:05	250	500×1024	$(12.9, -8.6)$	1915.0578	1.60	-0.193
2b	1996 Oct 18, 21:25	300	500×1024	$(12.8, 7.3)$	1915.0945	1.62	-0.280
2c	1996 Oct 20, 08:51	180	500×1024	$(12.6, 7.9)$	1915.1678	1.65	0.034
3	1997 Jan 16, 22:33	90	1024×250	$(1.44, 0.6)$	1918.3942	1.52	0.063

[a]Nominal five minute step cadence.

[b]Horizontal × vertical.

[c]At start of tracking sequence.

[d]Heliocentric latitude, longitude.

3.2. Labelling & Tracking

Having smoothed the data and estimated the error per pixel, we then used a novel, single-pass “flux-ranked uphill gradient” (Longcope 2000) algorithm to group and label pixels into flux elements, which we define to be convex groupings of 10 or more unipolar, contiguous pixels, with field strength greater than 10 G in absolute value.

In outline, the algorithm:

1. ranks pixels’ field strengths’ absolute values from highest to lowest, down to the 10 G threshhold, and labels each pixel with its rank;

2. proceeds from the highest to the lowest label, at each step comparing the field strengths of each pixel with its 8 nearest neighbors, and determining which of these 9 pixels has the strongest field;

3. gives the central pixel the label of that pixel with the highest field strength.

Hagenaar et al. (1999) used object selection criteria very similar to ours, but with the added constraint that the peak field strength, B_{MAX}, in each flux element had to exceed 30 G. We found similar flux element densities ($\rho_\Phi \sim (2.5 - 3) \times 10^{-9}\mathrm{km}^{-2}$), and, also like them, exponential distributions for elements’ total fluxes, $f(\Phi_0) \propto \exp -\Phi/\Phi_0$, over a limited range of flux values. Our fitted values for Φ_0 were in the range of $2.8 - 3.6 \times 10^{18}$ Mx. In addition, we also found exponential distributions for the flux elements’ sizes, and average and maximum field strengths.

The flux elements defined by the labelling algorithm described above have been tracked from one five-magnetogram average to the next. Following Hagenaar et al. (1999), we adopt *overlap* as the basic rule for associating flux elements from different time steps. As differing assumptions in tracking algorithms can lead to differing results, we discuss our algorithm in detail in appendix A.

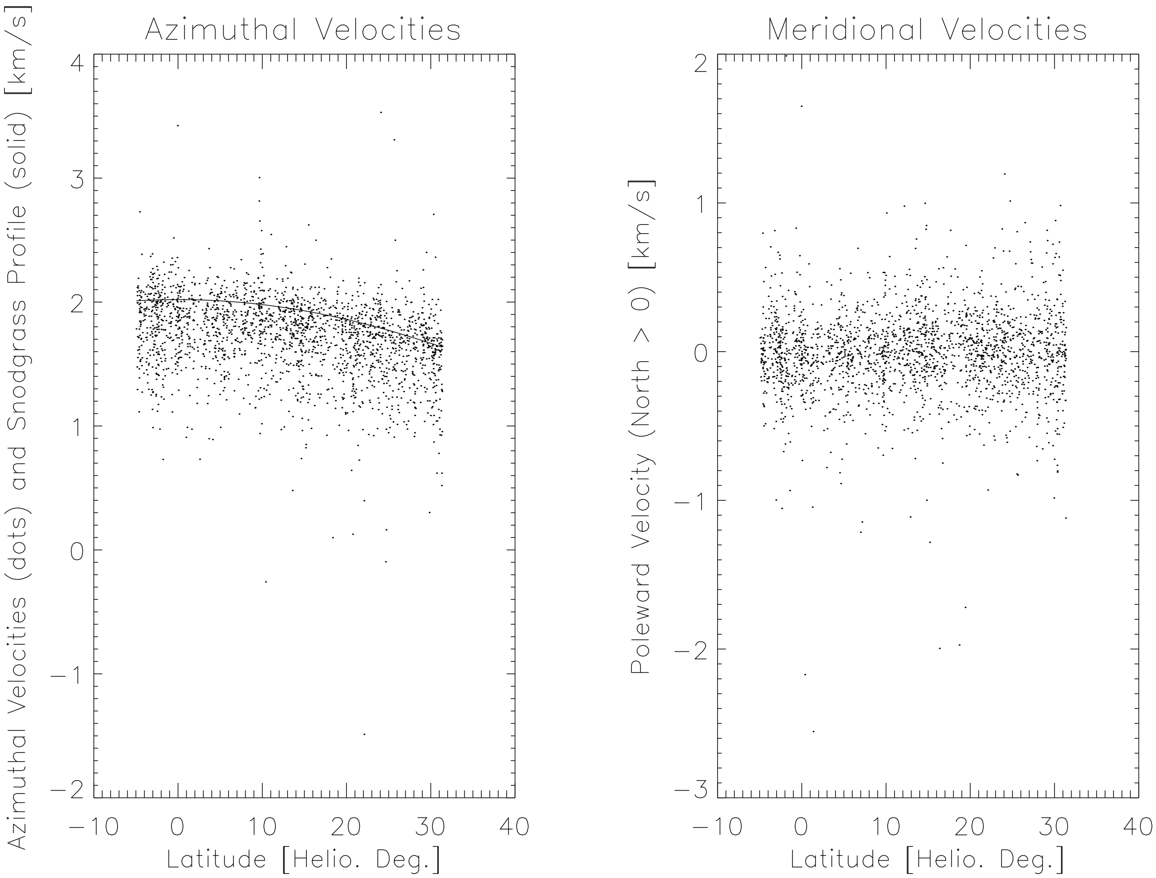

Fig. 2.— Plotted rotational (left) and meridional velocities (right), as a function of heliographic latitude in data set # 2a. The Snodgrass (1983) differential rotation profile is shown in the left plot. Plots for other data sets look similar.

To verify that the tracking algorithm works as expected, we plot the tracked rotational and meridional velocities for each data set in Figure 2. The latitudinal variation in our fluxes' sidereal rotation speeds is similar to that in the published differential rotation profile of Snodgrass (1983), obtained by correlation averaging daily full-disk magnetograms from Mt. Wilson. The average and median meridional speeds, at a few meters per second northward, are of the same order of magnitude as published values for meridional motions of sunspots (Howard and Krishnamurti 1986), but are well below published flow rates of tens of meters/second inferred from helioseismology (Gonzalez *et al.* 1999).

3.3. Finding the Mutual Helicity Flux

We use equation (10) to find the helicity flux from each pair of fluxes a, b in the time interval $\Delta t_{k+1,k}$ between t_k and t_{k+1}. Averaged values from t_k and t_{k+1} are used for Φ_a and Φ_b. We find Ω_{ab} by calculating the angular separation between the vector $\mathbf{r}_{ab,k}$ that runs between Φ_a and Φ_b at time t_k, and the vector $\mathbf{r}_{ab,k+1}$ that links the two at t_{k+1}, and dividing this angular displacement by $\Delta t_{k+1,k}$. Finally, the total helicity flux is found by summing that from all pairs.

4. Results

4.1. Mutual Helicity

In Table 2, we summarize the statistical properties of the measured fluxes of mutual helicity from the data sets. Values in the first four columns are per FOV. In the first column, we show the unweighted average of the mutual helicity flux for each set,

$$\langle d\mathcal{H}/dt\rangle_t = \sum_{k=1}^{N_t}\Big(d\mathcal{H}_k/dt\Big)\Big/\sum_{k=1}^{N_t}(1) = \frac{1}{N_t}\sum_{k=1}^{N_t}\Big(d\mathcal{H}_k/dt\Big) \quad , \tag{14}$$

and the square root of the variance of the helicity flux, s. The subscript t on the angle brackets denotes an average over time: the summation index, k, is summed over the number of time steps, N_t, in each tracking run.

To account for measurement errors, we also calculate the average mutual helicity flux for each data set using instrumental weighting,

$$\langle d\mathcal{H}/dt\rangle_\sigma = \sum_{k=1}^{N_t}\Big[(d\mathcal{H}_k/dt)/\sigma_k^2\Big]\Big/\sum_{k=1}^{N_t}(1/\sigma_k^2) \tag{15}$$

and its average error,

$$1/\bar{\sigma}^2 = \sum_{k=1}^{N_t} (1/\sigma_k^2) \quad , \tag{16}$$

by weighting with the measured errors, which we denote with the subscript σ on the angle brackets. The errors were computed by differentiating our expression for the helicity flux with respect to the measured magnetic fluxes, multiplying by the errors in magnetic fluxes, and adding the results in quadrature. We estimated the error in magnetic flux for each element using the per-pixel noise σ_n (from the final column of Table 1) to be $\sqrt{N}\sigma_n A$, where N is the flux element size, in pixels, and A is the area per pixel.

Table 2. Mutual Helicity Fluxes

Data Set	$\langle d\mathcal{H}/dt\rangle_t \pm s$[a] ($10^{33}$Mx^{2}s^{-1})	$\langle d\mathcal{H}/dt\rangle_\sigma \pm \bar{\sigma}$[a] ($10^{33}$Mx^{2}s^{-1})	median$(d\mathcal{H}/dt)$[a] (10^{33}Mx^{2}s^{-1})	$\langle d\mathcal{H}/dt\rangle \pm \sigma$ (10^{13}Mx^{2}cm^{-2}s^{-1})
1	$-.443 \pm 80.63$	$-.0187 \pm 4.29$	-6.85	-0.00234 ± 0.537
2a	-10.2 ± 328	-3.26 ± 5.34	6.39	-0.326 ± 0.532
2b	-41.7 ± 313	-16.1 ± 4.79	-2.75	-1.61 ± 0.479
2c	-93.5 ± 590	-116 ± 13.5	-86.2	-11.6 ± 1.35
3	-9.78 ± 48.0	-5.92 ± 1.99	-6.09	-1.18 ± 0.398

[a]Integrated over FOV.

Both methods of finding the average mutual helicity flux give negative average fluxes in all runs. Both methods also yield relatively small values for data set 1, and relatively large values for data set 2c, which differ from each other by more than two orders of magnitude using either method. In most of the data sets, the weighted average values for the mutual-helicity flux are smaller than the unweighted averages. This implies that the errors in the helicity fluxes are larger for larger helicity fluxes, diminishing their contribution to the weighted average.

Both methods of averaging to estimate the mean mutual helicity flux might be dominated by a few large values of helicity flux of either sign. To check if such a bias is present, we also computed the median value of the helicity flux time series for each tracking run, which is given in the third column of the table. In most cases, the median value is the on same order of magnitude as the averaged values.

To account for the different fields of view in the data sets (see Table 1), we have also calculated the mutual helicity flux density, and its error, by normalizing the weighted-average helicity flux and its error in each tracking run by the area of the FOV in that run. The results are in the final column of the table.

The table indicates that a typical absolute value of the mutual helicity flux for a MDI FOV is $\sim -10^{33}\mathrm{Mx}^2\mathrm{s}^{-1}$, while a typical flux density is $\sim -10^{13}\mathrm{Mx}^2\mathrm{cm}^{-2}\mathrm{s}^{-1}$.

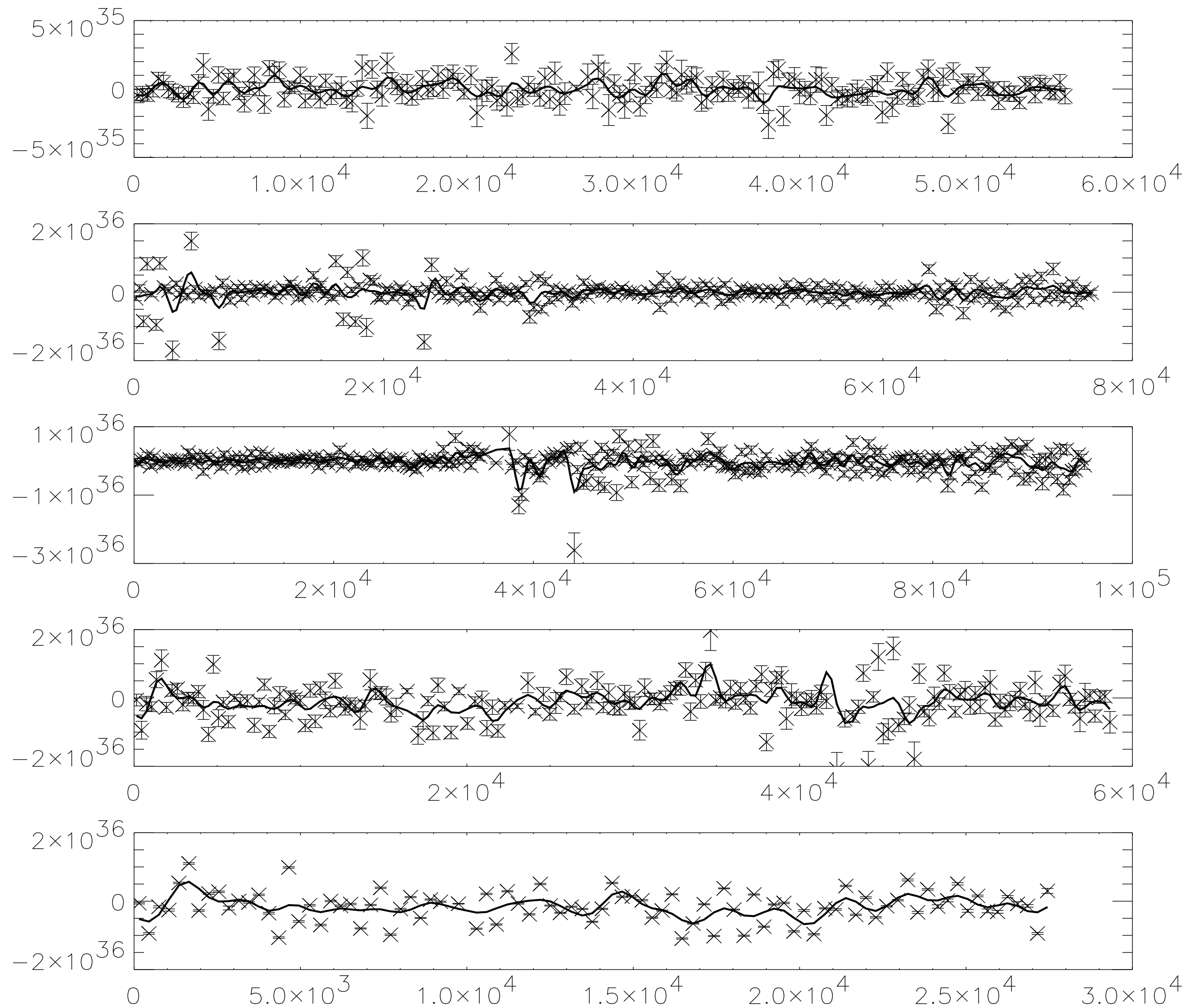

Fig. 3.— Mutual helicity flux as a function of time in data sets (top to bottom) 1, 2a, 2b, 2c, and 3. Abscissae are in seconds, ordinates are in $\mathrm{Mx}^2\mathrm{s}^{-1}$. Note differing scales. Solid lines result from smoothing the time series.

We plotted the time series of mutual helicity flux in all five tracking runs in Figure 3; note the differing scales. In each plot of the helicity flux, the solid line is the helicity flux after low-pass filtering. The time series exhibit large fluctuations, but the sets' fourier transforms share no obvious features.

Most of the error bars are smaller than the excursions of the helicity flux from zero, meaning the measured helicity flux in each data set is not consistent with zero helicity flux. To quantify this, we calculated the value χ^2 over each data set of N_t measurements, assuming a zero-flux model, and computed the value $P(\chi^2_{\rm obs}|N_t)$, the probability that, given N_t degrees of freedom, a correct model's $\chi^2_{\rm model}$ would be less than $\chi^2_{\rm obs}$. In every data set, $P(\chi^2_{\rm obs}|N_t) = 1$, implying the zero-flux model with Gaussian deviations of sizes equal to σ_k, the measurement error at each time step, is ruled out.

A different model, in which the the data were assumed to be Gaussian excursions of size σ_k about the mean helicity flux, $\langle d\mathcal{H}/dt\rangle_t$, was also ruled out by a similar analysis in every data set.

We conclude that the mutual helicity flux density in the quiet sun for our data sets is predominantly negative but intrinsically variable, with an approximate amplitude given by the typical standard deviation in the helicity flux density, $\sim 5\times10^{12}{\rm Mx^2cm^{-2}s^{-1}}$.

4.2. Contributions to Helicity Flux

In Section 2.3, we predicted that the mutual helicity flux would be greater than zero. In every dataset, however, we found the flux to be negative. To understand our results, we investigated the contributions of the relative angular velocities of the flux elements and their fluxes to the total mutual helicity flux given by equation (8).

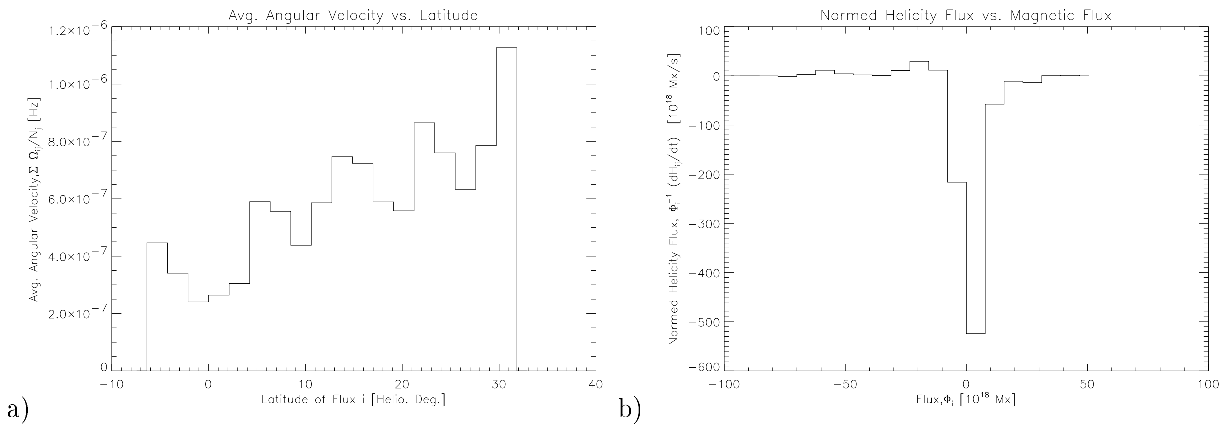

Fig. 4.— a) The average rotation rate of all other elements about each element, averaged in latitude bins, shows that the sense of relative rotation in data set # 2b is positive. b) The normed mutual helicity contribution from each element i, due to the motions of all other elements, as a function of Φ_i, confirms that most of the mutual helicity in data set # 2b arises from the smallest fluxes, which comprise a majority of the population.

We expected, from the differential rotation profile in the mostly-northern latitudes of our data sets, that the average sense of relative rotation between flux elements would be right-handed. To check this, we binned the flux elements by latitude, computed the average angular rotation of other fluxes about each flux in each time step, and plotted the average value in each bin for each data set. An example plot is shown in Figure 4 a). Only in data set 3 is the average of the angular velocities not positive, probably because the differential rotation acts weakly at the low latitudes of its coverage. Hence, we conclude that, as predicted, flux elements rotated about each other in a predominantly positive sense.

Since the measured angular velocities are quite small, but some of the flux elements contain relatively large amounts of flux, we also considered the possibility that the mutual helicity flux signal was dominated by small, random relative motions in pairings of large fluxes. To investigate this, we calculated the mutual helicity contributions attributable to a single element i, due to the motions of all other elements. Plots of this contribution as a function of Φ_i, such as the example in Figure 4 b), show the largest contribution to the total helicity comes from the smallest fluxes, which comprise the majority of the population. Evidently, the total mutual helicity flux distribution was not dominated by the relatively few high-flux elements.

The discrepancy between our predicted and measured flux rates probably arises from our assumption that $N_+ = N_-$ in our theoretical calculation. If we relax this assumption and repeat the analysis that led to equation (11), we find the coefficient H_0 becomes

$$H_0 = 2\Phi_0^2[N - (\Delta N)^2/2]/\pi \quad , \tag{17}$$

where $N = (N_+ + N_-)/2$ and $\Delta N = (N_+ - N_-)$. Hence, for $|\Delta N| \geq \sqrt{2N}$, the sign of H_0 flips.

In fact, the tracked polarities' imbalance in both number and flux in the first five-magnetogram average in every data set is great enough to explain the sign discrepancy. In sets # 1,2a,2b,2c, and 3, the population imbalances, ΔN, for the tracked fluxes were 27,-26,-53,104, and 37, respectively, while the rounded values of $\sqrt{2N}$ were 19,22,23,24, and 15. And the flux imbalances, divided into units of our characteristic quantum of flux, $\Phi_0 = 3 \times 10^{18}$ Mx, corresponded to 39,-66,-69, 237, and 35 of these flux units, respectively. We note that data set # 2c had both the largest flux imbalance and the most-negative helicity flux rate (see Table 2), in accordance with the quadratic dependence on ΔN in equation (17).

We hypothesize that ΔN would vanish in a summation over all quiet-sun fluxes in the northern hemisphere, which, combined with the observed right-handed relative rotation there, would yield a positive flux of helicity.

5. Conclusions

The quiet sun mutual helicity flux fluctuates rapidly, but in a manner inconsistent with Gaussian measurement deviations about a mean mutual helicity flux rate equal either to zero or to the average flux rate in each tracking run. From the flux imbalances present in all data sets, the average mutual helicity flux in all sets is negative, and on the order of $\sim -5 \times 10^{12}\mathrm{Mx^2cm^{-2}s^{-1}}$, though fluctuations ranged almost three orders of magnitude higher in amplitude. Our prediction for the average mutual helicity flux was in the range of $10^{11}\mathrm{Mx^2cm^{-2}s^{-1}}$, opposite in sign and roughly an order of magnitude smaller than the observed average flux rates in the data set.

The temporal coverage of our data sets is limited, and falls near the minimum of the solar cycle. Nonetheless, we can make an order-of-magnitude estimate of the absolute value of the whole-cycle, quiet-sun flux of mutual helicity from our results. Multiplying our unsigned helicity flux density by the length of a cycle gives

$$\mathcal{H}_{\mathrm{cyc}} \sim 10^{21}\mathrm{Mx^2cm^{-2}} \tag{18}$$

through the lower latitudes ($< 30°$ heliocentric) of the northern hemisphere over an 11 year cycle.

With the caveat that the unipolar nature of the weak polar fields might cause the actual absolute helicity flux density to increase greatly toward the poles (as the flux imbalance increases), we can extrapolate our results to include the polar regions, which gives a whole-cycle helicity flux of

$$\mathcal{H}_{\mathrm{cyc}}^{(\mathrm{NH})} \sim 10^{43}\mathrm{Mx^2} \tag{19}$$

through the northern hemisphere.

Published estimates of the flux of helicity from active regions (Demoulin *et al.* 2002a; Green *et al.* 2002; DeVore 2000) suggest that $\sim 10^{43}\mathrm{Mx^2}$ of helicity (or more) can come from a single active region. Hence, the contribution to the Sun's total helicity budget from braiding of quiet sun fluxes is negligible compared to the contribution from active region fields, assuming $\sim 10^3$ active regions emerge per cycle.

Considering that the cycle-integrated magnetic fluxes in quiet sun fields and active region fields are commensurate (both on the order of 10^{25} Mx), it is surprising that the observed quiet-sun mutual helicity flux is three orders of magnitude less than the active region helicity flux.

But we have not considered all the terms in the full expression for the quiet-sun helicity flux here. In another paper, currently in preparation, we present measurements of the quiet-sun self-helicity flux rate from braiding motions. And the emergence of quiet-sun fields already containing helicity through the photosphere, which we neglected when we dropped the left term of equation (2), might make a significant contribution to the Sun's helicity budget. We note that the high spatial resolution, high cadence, long-duration observations of the quiet-sun vector magnetic field that should be possible with the focal plane package (FPP) on the Solar B mission (now scheduled for launch in 2005) might allow quantitative estimation of the quiet-sun helicity emergence rate.

A. Tracking Algorithm

For two fluxes to overlap in our tracking algorithm, the centers of flux of two elements, labelled a and b, at times t_k and t_{k+1}, respectively, must lie within $r_{\rm size}$ pixels of each other, where

$$r_{\rm size} \equiv \sqrt{\max\{{\rm size}(a), {\rm size}(b)\}}\ . \tag{A1}$$

In words, $r_{\rm size}$ is the square root of the area of the flux element of the greatest size, in pixels. This approach is ideally suited for high-cadence measurements of features of finite extent, but is not suited to low-cadence data sets, or to tracking point-like features, e.g., G-band bright points.

To search for matches between a flux elements at time t_k and fluxes from an adjacent time t_ℓ, with $\ell = k \pm 1$, the first algorithm we use finds the five nearest-neighbor fluxes from t_ℓ for every flux from t_k, and determines which overlap. The procedure is then repeated with the roles reversed.

The next routine sorts through the nearest neighbor arrays to determine each flux's relation to the fluxes in the adjacent time step. In terms of fluxes from these old and new sets, there are only five possibilities:

1. *disappearance* of an old flux;

2. *appearance* of a new flux;

3. *one-to-one* matches between one old and one new flux;

4. *collisions* of old fluxes, to produce one new flux;

5. *fragmentations* of one old flux, to produce new fluxes.

We note that collisions and fragmentations always involve fluxes of the same sign.

A flux from the earlier time step which has no overlapping counterpart in the later time step is labelled as a *disappearance*. An *appearance* occurs in an analogous fashion, when a flux from the later time step has no overlapping counterpart in the earlier.

Ideally, each instance of the disappearance/appearance of flux of a given sign could be matched with an equivalent change of flux of the opposite sign, as a natural consequence of the divergence-free nature of magnetic fields. In practice, however, our tracking method can lead ambiguities in interpreting the appearance or disappearance of flux: field strengths could randomly decrease below our 10 G threshhold (by turbulent diffusivity, for instance), and flux elements can wander in and out of the field of view. Hence, there is not always an obvious physical interpretation to the disappearance/appearance of a labelled flux element in our data sets.

Flux elements which *mutually* overlap are candidates for some type of matching: one-to-one, collision, or fragmentation. In relatively empty regions where flux elements are widely separated, fluxes may have only one overlap, and may be each other's nearest neighbors; if so, they are obviously a one-to-one match. After finding submergences and emergences described above, the matching algorithm looks for just such clear-cut cases of one-to-one matches. In crowded regions, where many fluxes may overlap, the matching algorithm still pairs mutual nearest neighbors as one-to-one. Other fluxes which remain unmatched after a first pass are then checked again. If they mutually overlap and are both unmatched, but one is not the other's nearest neighbor, they are still matched one-to-one.

Flux elements still not matched but which *do* mutually overlap with some already-matched flux element from the adjacent time step are either labelled a collision or a fragmentation. A collision occurs when two or more flux elements from the old time step overlap one from the new time. The sizes of the parent fluxes are compared and the child takes the label of the larger parent. A fragmentation occurs with the roles reversed: two or more new flux elements overlap one old flux, and the larger child takes the parent's label.

The processes described above must satisfy equations of detailed balance in each step of the tracking. These equations relate the numbers of flux elements at the new and old time steps ($N_{\rm new}$ and $N_{\rm old}$, respectively), to the numbers propagated ($N_{\rm oto}$), created ($N_{\rm app}+N_{\rm frag}$), and destroyed ($N_{\rm disapp}+N_{\rm coll}$):

$$N_{\rm new} = N_{\rm old} + N_{\rm app} + N_{\rm frag} - N_{\rm disapp} - N_{\rm coll} \tag{A2}$$

$$N_{\rm new} = N_{\rm oto} + N_{\rm app} + N_{\rm frag} \tag{A3}$$

$$N_{\rm old} = N_{\rm oto} + N_{\rm disapp} + N_{\rm coll} \quad . \tag{A4}$$

The tracking routine stops with an error flag if any of these constraints are violated at any tracking step. In practice, about 90% of flux elements are matched one-to-one in each tracking step.

Statistics on appearance, disappearance, collision, and fragmentation rates were compiled. Our collision and framentation rates were higher than those of Hagenaar et al. (1999), which is probably a result of differing definitions of collisions and fragmentations in our tracking algorithms.

The authors acknowledge the anonymous referee, whose comments led to an improved manuscript. This work was supported in part by NSF grant ATM-9733424, in part by NASA grant NAG5-6110, and in part by the Institute for Theoretical Physics, which is supported by NSF grant PHY99-07949. We thank the American public for its generous support of these agencies, and, ultimately, our work.

REFERENCES

Berger, M. 1999, Magnetic Helicity in Space Physics, in *Magnetic Helicity in Space and Laboratory Plasmas*, pp. 1–9, AGU.

Berger, M. A. and Field, G. B. 1984, JFM 147, 133.

Boozer, A. H. 1999, Implications of Magnetic Helicity Conservation, in *Magnetic Helicity in Space and Laboratory Plasmas*, pp. 11 – 16, American Geophysical Union.

Chae, J. 2001, ApJ 560, L95.

Demoulin, P., Mandrini, C. H., van Driel-Gesztelyi, L., Thompson, B. J., Plunkett, S., Kővári, Z., Aulanier, G., and Young, A. 2002a, A&A 382, 650 .

Demoulin, P., Mandrini, C. H., van Driel-Gesztelyi, Lopez Fuentes, M., and Aulanier, G. 2002b, Solar Phys. 207, 87 .

DeVore, C. R. 2000, ApJ 539, 944 .

Finn, J. and Antonsen 1985, Commments of Plasma Physics and Controlled Fusion 9, 111.

Gonzalez, H. I., Patron, J., Bogart, R. S., and Team, T. S. R. D. 1999, ApJ 510, L153.

Green, L. M., Lopez Fuentes, M. C., Mandrini, C. H., Demoulin, P., van Driel-Gesztelyi, L., and Culhane, J. L. 2002, Solar Phys. , in press.

Hagenaar, H., Schrijver, C., Title, A., and Shine, R. 1999, ApJ 511, 932.

Howard, L. H. and Krishnamurti, R. 1986, JFM 170, 385.

Kusano, K., Maeshiro, T., Yokoyama, T., and Sakurai, T. 2002, ApJ 507, 501 .

LaBonte, B. J. and Howard, R. 1982, Solar Phys. 80, 15.

Rust, D. 2002, Magnetic helicity, coronal mass ejections and the solar cycle, in *Proceedings of the Second Solar Cycle and Space Weather Euroconference*, volume SP-477, pp. 39–41, Noordwijk, ESA.

Scherrer, P., Bogart, R. S., Bush, R. I., Hoeksema, J. T., Kosovichev, A., Schou, J., Rosenberg, W., Springer, L., Tarbell, T., Title, A., Wolfson, C., Zayer, I., and TEAM, T. M. E. 1995, Solar Phys. 162, 129 .

Schrijver, C. J., Title, A. M., van Ballegooijen, A. A., Hagenaar, H. J., , and Shine, R. A. 1997, ApJ 487, 424 .

Smith, C. W. 1999, Solar-Cycle, Radial, and Latitudinal Variations of Magnetic Helicity: IMF Observations, in *Magnetic Helicity in Space and Laboratory Plasmas*, pp. 239–245, American Geophysical Union.

Snodgrass, H. 1983, ApJ 270, 288.

Taylor, J. B. 1974, Phys. Rev. Lett. 33(19), 1139.

Zirker, J. B., Martin, S. F., Harvey, K. H., and Gaizaukas, V. 1997, Solar Phys. 175, 27.

This preprint was prepared with the AAS LaTeX macros v5.0.